Geomorphology 237 (2015) 130–141

Contents lists available at ScienceDirect

Geomorphology

journal homepage: www.elsevier.com/locate/geomorph

Slip distributions on active normal faults measured from LiDAR and field mapping of geomorphic offsets: an example from L'Aquila, Italy, and implications for modelling seismic moment release

Maxwell Wilkinson [a,c,*], Gerald P. Roberts [b], Ken McCaffrey [c], Patience A. Cowie [d], Joanna P. Faure Walker [e], Ioannis Papanikolaou [f], Richard J. Phillips [g], Alessandro Maria Michetti [h], Eutizio Vittori [i], Laura Gregory [g], Luke Wedmore [e], Zoë K. Watson [e]

[a] Geospatial Research Ltd., Suites 7 & 8, Harrison House, Hawthorn Terrace, Durham, DH1 4EL UK
[b] Department of Earth and Planetary Sciences, Birkbeck, University of London, London, WC1E 7HX UK
[c] Department of Earth Sciences, South Road, Durham University, Durham, UK DH1 3LE
[d] University of Bergen, Department of Earth Science, P.O. Box 7803, N-5020 Bergen, Norway
[e] Institute for Risk and Disaster Reduction, Earth Sciences, UCL, University of London, WC1E 7HX UK
[f] Laboratory Mineralogy – Geology, Agricultural University of Athens, Greece
[g] School of Earth and Environment, University of Leeds, Leeds, LS2 9JT UK
[h] Dipartimento di Scienza e Alta Tecnologia, Via Valleggio 11, 22100, Como, Italy
[i] Servizio Geologico d'Italia, ISPRA, Via Vitaliano Brancati, 48-00144, Roma, Italy

ARTICLE INFO

Article history:
Received 15 June 2012
Received in revised form 5 March 2014
Accepted 12 April 2014
Available online 2 May 2014

Keywords:
Earthquake slip distribution
Fault scarps
Last glacial maximum
LiDAR

ABSTRACT

Surface slip distributions for an active normal fault in central Italy have been measured using terrestrial laser scanning (TLS), in order to assess the impact of changes in fault orientation and kinematics when modelling subsurface slip distributions that control seismic moment release. The southeastern segment of the surface trace of the Campo Felice active normal fault near the city of L'Aquila was mapped and surveyed using techniques from structural geology and using TLS to define the vertical and horizontal offsets of geomorphic slopes since the last glacial maximum (15 ± 3 ka). The fault geometry and kinematics measured from 43 sites and throw/heave measurements from geomorphic offsets seen on 250 scarp profiles were analysed using a modification of the Kostrov equations to calculate the magnitudes and directions of horizontal principal strain-rates. The map trace of the studied fault is linear, except where a prominent bend has formed to link across a former left-stepping relay-zone. The dip of the fault and slip direction are constant across the bend. Throw-rates since 15 ± 3 ka decrease linearly from the fault centre to the tip, except in the location of the prominent bend where higher throw rates are recorded. Vertical coseismic offsets for two palaeo earthquake ruptures seen as fresh strips of rock at the base of the bedrock scarp also increase within the prominent bend. The principal strain-rate, calculated by combining strike, dip, slip-direction and post 15 ± 3 ka throw rate, decreases linearly from the fault centre towards the tip; the strain-rate does not increase across the prominent fault bend. The above shows that changes in fault strike, whilst having no effect on the principal horizontal strain-rate, can produce local maxima in throw-rates during single earthquakes that persist over the timescale of multiple earthquakes (15 ± 3 ka). Detailed geomorphological and structural characterisation of active faults is therefore a critical requirement in order to properly define fault activity for the purpose of accurate seismic hazard assessment. We discuss the implications of modelling subsurface slip distributions for earthquake ruptures through inversion of GPS, InSAR and strong motion data using planar fault approximations, referring to recent examples on the nearby Paganica fault that ruptured in the Mw 6.3 2009 L'Aquila Earthquake.

1. Introduction

The spatial distribution of geomorphic offsets across active normal faults reveal that surface fault traces are non-linear features, characterised by discontinuities such as relay zones and bends in the fault trace (Faure Walker et al., 2009). It is well-known that surface

* Corresponding author.
E-mail address: max@geospatial-research.co.uk (M. Wilkinson).

http://dx.doi.org/10.1016/j.geomorph.2014.04.026

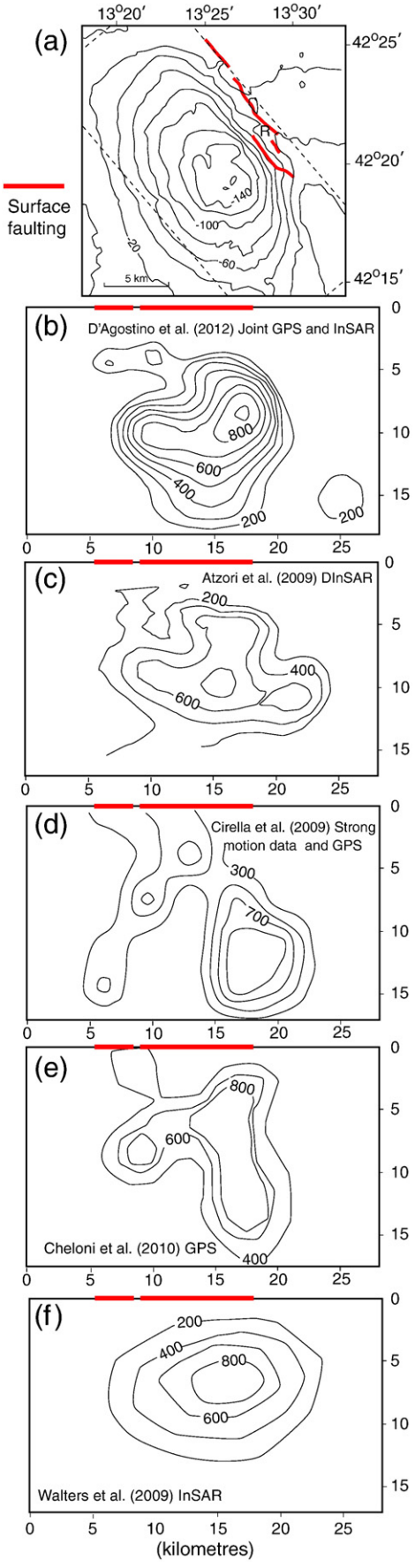

ruptures to individual earthquakes can follow these discontinuities, wrapping around small-scale bends in the fault trace and crossing relay zones (Roberts, 1996a, 1996b; Wesnousky, 2006). This implies that at depth the fault may be continuous across such small-scale surface discontinuities. Although the surface slip distribution can be examined by geomorphologists, in contrast, the subsurface slip distribution can only be inferred through inversion of seismological and geodetic data, and then only for that particular earthquake (Fig. 1). This paper examines the possible effects of bends and relay zones measured at the surface on subsurface slip distributions. The subsurface slip distribution is important for two reasons: (1) it defines the ruptured area and amount of slip, which alongside the stiffness of the deforming material define the seismic moment, or energy release in an earthquake (Kostrov, 1974; Wells and Coppersmith, 1994); (2) it is used to model how stress is transferred onto fault surfaces that were not ruptured in that particular earthquake, but could represent the sites of future earthquake rupture (e.g. Walters et al., 2009). In this paper we show that although the subsurface slip-distribution is beyond the direct observation of geomorphologists, geomorphic observations of the surface slip distribution can provide fundamental constraints on these earthquake processes.

In particular, Faure Walker et al. (2009) showed that cumulative offsets of dated geomorphic surfaces across fault scarps, combined with measurements of the strike and dip of the fault plane and plunge and plunge direction of the slip vector from slickensides, can be used to derive the relationship between: (1) the vertical and horizontal motions of the rocks around the fault; (2) the amount of slip on the fault plane; (3) the strain-rates implied by such motions, and how these relate to regional strain-rates imposed by motions between and within tectonic plates. In order to maintain the imposed strain-rate at locations where bends in the strike of normal faults exist, Faure Walker et al. (2009) described the theoretical basis for the fact that the rate of throw accumulation must increase relative to the rest of the fault, because vertical and horizontal motions, slip on the fault and strain rates are inter-related (see Methods section, below). Faure Walker et al. (2009) described the theory, but the need for more detailed observations was highlighted; this paper provides this by describing a bend in the Campo Felice Fault.

We point out that despite knowledge of the theoretical effects of changes in the orientation of faults on slip-distributions, normal faulting earthquake slip is commonly modelled assuming planar fault geometries without considering bends in the fault trace, even where such features are evident from the fault-related geomorphology. For example, a number of authors have attempted to invert data from seismology, GPS and InSAR collected over a time period encompassing the Mw 6.3 2009 L'Aquila Earthquake in Italy (Fig. 1; Atzori et al., 2009; Cirella et al., 2009; Walters et al., 2009; Cheloni et al., 2010; D'Agostino et al., 2012). The ground deformation around the Paganica Fault that ruptured in 2009 has been used to iteratively-model the subsurface slip, utilising elastic half-space dislocation models. Modelling is facilitated by assumptions concerning the shear modulus, Poisson's ratio and rheological layering. A common feature of these models is that a planar fault is assumed without including mapped bends in the fault trace. The simplified planar fault is then discretised into small (~1 × 1 km) patches from the larger fault surface (~25 × 15 km). Measured ground deformation of the earth's surface are then modelled iteratively by varying the subsurface slip-distribution on this simplified planar fault. Solutions vary between different authors for this type of modelling (Fig. 1). However, a common feature of all these interpretations is that the maxima in

Fig. 1. Map of surface deformation and modelled subsurface slip distributions for the 2009 Mw 6.3 L' Aquila earthquake, Italy. (a) Surface ruptures adapted from Boncio et al. (2010) with contours of "coseismic" surface displacements recorded by InSAR between 4th April 2009 and 12th April 2009 adapted from D'Agostino et al. (2012). Dashed line approximates the modelled planar, rectangular faults in panels b-f. (b)-(f) Range of modelled slip distributions from different combinations of InSAR, GPS and strong motion data. Heavy lines on b-f show the extent of surface faulting from Boncio et al. (2010). Note the relative positions of the maximum value for surface deformation and subsurface slip distributions; these maxima are skewed towards the southeastern tip of the surface ruptures.

subsurface coseismic slip underlies the area where greatest coseismic subsidence was measured at the surface. We point out that this maximum in subsidence and modelled slip is skewed in location towards the SE end of the fault where it is known that the surface ruptures stepped to the right, defining a 1–2 km across relay zone (labelled R in Fig. 1a) (compare Fig. 1a with b–e). In this paper we examine the relationship between such relay-zones, slip on the fault plane at depth and vertical motions of the ground surface. We suggest, following Faure Walker et al. (2009), that the relay zone may overlie a zone of non-planarity in the fault plane at depth that may have induced anomalous surface deformation. This is important because Calderoni et al. (2012) have suggested from an analysis of fault-trapped seismic waves for the 2009 earthquake that the discontinuous fault segments at the surface are part of a continuous fault system at depth. Unfortunately, the Paganica Fault is poorly-exposed relative to other nearby faults and thus the geomorphic signature of slip and fault kinematics are difficult to retrieve, so we have been unable to directly apply the theory from Faure Walker et al. (2009). Thus, to quantify how much the vertical deformation is affected by relay zones or bends in the fault trace, we utilise observations of a well-exposed fault located ~15 km to the south southwest of the faults that ruptured in 2009 – the Campo Felice active normal fault.

The Campo Felice fault exhibits a well-exposed bedrock fault scarp that records slip since the last-glacial maximum (15 ± 3 ka, as supported by Giraudi et al., 2011; Giraudi, 2012). The fault displays clear evidence of coseismic slip due to past earthquakes in the form of strips of freshly-exposed rock at the base of the fault plane (see Giaccio et al., 2002). The relationship between vertical motions, slip on the fault and strain-rate can be retrieved across a prominent fault bend because the fault plane is well-preserved and exhibits numerous examples of slickenside surfaces covered in frictional-wear striae that record the slip vector orientation. We have measured the orientations of the fault plane and slip-vector in the field, and studied the geomorphology of the site using terrestrial laser-scanning (TLS) in order to retrieve the slip distribution and throw recorded by offset geomorphology along strike. Similar approaches also exist for the study of offset geomorphic features within extensional basins and for strike-slip and reverse faults from LiDAR data (see Chan et al., 2007; Oldow and Singleton, 2008; Zielke et al., 2010; Gold et al., 2011, 2012; Zielke and Arrowsmith, 2012; Wiatr et al., 2013). This is the first time the approach has been applied in detail for a normal fault with analysis of how this relates to strain-rates computed from surface structural geology. We use the measurement of throw on the Campo Felice fault to discuss the likely patterns of slip at depth on the neighbouring Paganica fault and to emphasise that the geomorphic study of fault geometry and offsets is essential for seismic hazard assessment.

2. Geological background

The central Apennines contains active normal faults, such as the Campo Felice, Parasano and Paganica faults discussed in this paper (Figs. 2 and 3; Galadini and Galli, 2000; Roberts and Michetti, 2004; Pace et al., 2006; Faure Walker et al., 2010). Extension during the Plio-Pleistocene has been located on the high topography of the Apennine mountains, the site of an older, submarine foreland thrust belt produced during Cretaceous-Miocene Alpine convergence (Cowie et al., 2013). The normal faults offset pre-rift Mesozoic and Tertiary carbonates and have produced localised inter-montane basins in their hanging walls. The extension is associated with uplift and formation of the topography of the Apennine mountains (D'Agostino et al., 2001; Faure Walker et al., 2012).

Active normal faulting in the central Apennines is associated with a long historical and palaeo seismic record of past earthquakes (Galli et al., 2008). Events like the 1915 Mw 6.9–7.0 Fucino earthquake (33,000 deaths) and the 2009 Mw 6.3 L'Aquila earthquake (309 deaths) ruptured faults that are relatively well-mapped with clear surface

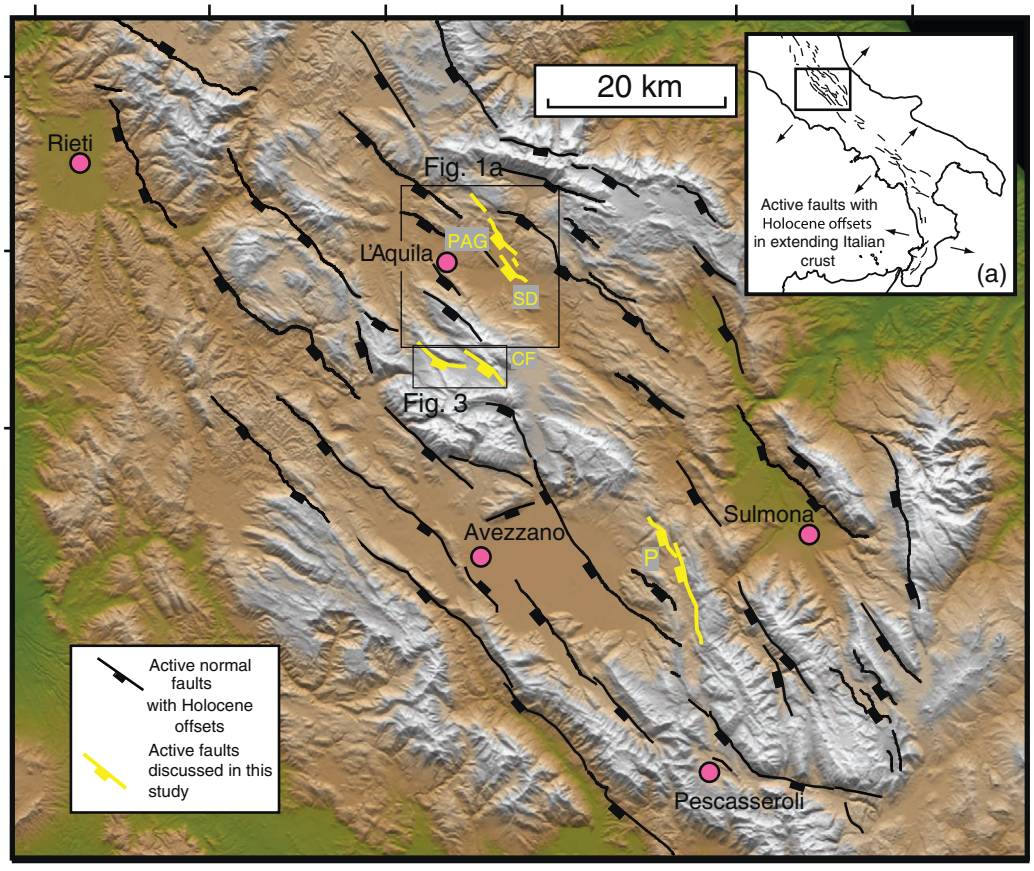

Fig. 2. Location map for active faults in central Italy on a 20 m DEM. Boxes locate Figs. 1 and 3. PAG – Paganica Fault, CF – Campo Felice Fault, P – Parasano Fault, SD – San Demetrio Fault.

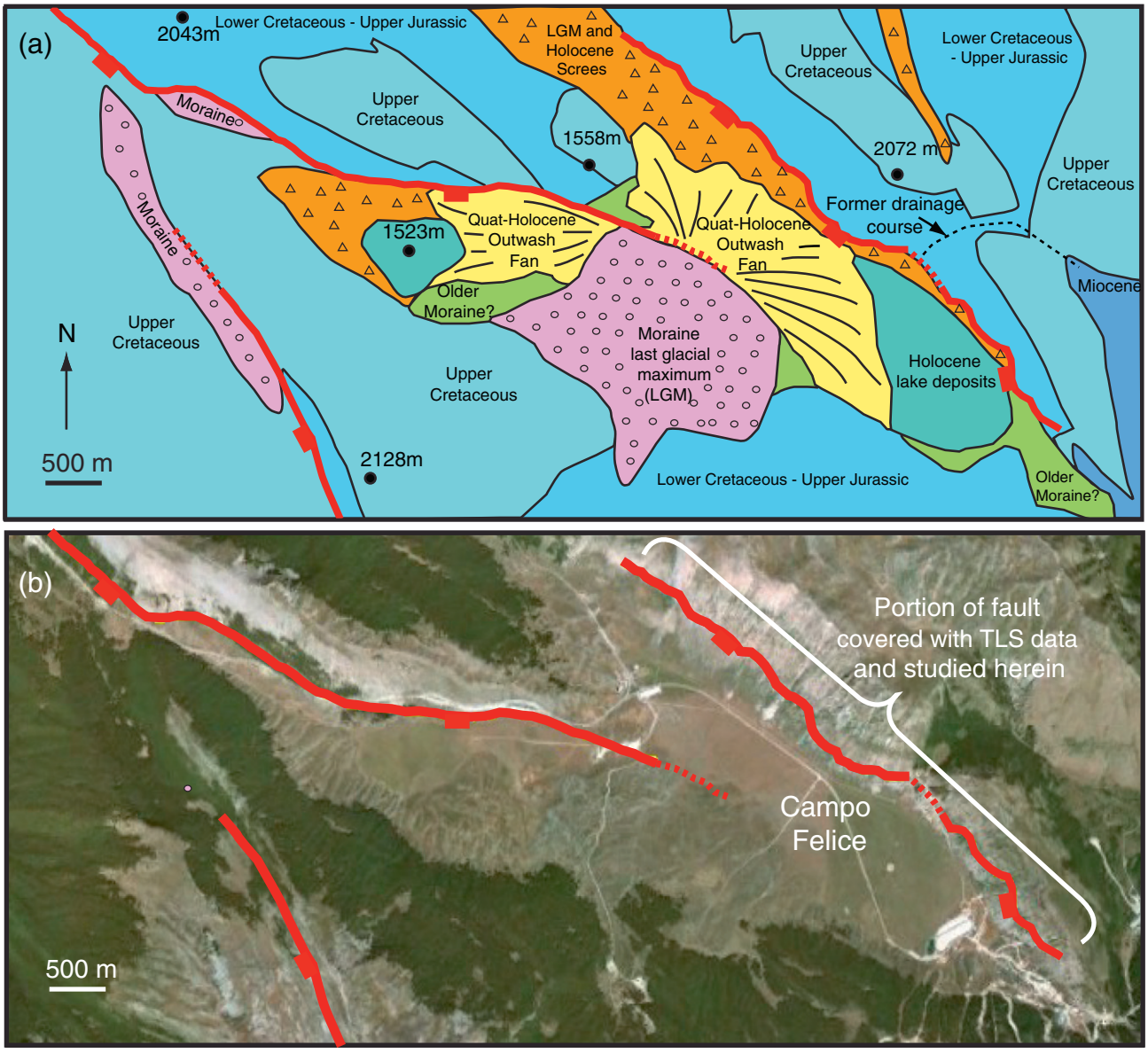

Fig. 3. Location maps for the Campo Felice fault. (a) Geological map adapted from Giaccio et al. (2002) and Vezzani and Ghisetti (1998). (b) Satellite imagery from Google Earth™. The faults offset Cretaceous carbonates with normal sense displacements, controlling the position of a Quaternary Holocene intra-montane basin, and have offset a former (Quaternary?) drainage course.

faulting (Michetti et al., 1996; Boncio et al., 2010). The L'Aquila earthquake ruptured the Paganica fault with surface vertical offsets of 10–15 cm through the town of Paganica, with continuation of the mapped ruptures both northwest and southeast of the town (see Papanikolaou et al., 2010; Vittori et al., 2011; D'Agostino et al., 2012 for reviews). Observations with InSAR and GPS demonstrate coseismic subsidence of up to 25 cm between 5–6 km into the hanging wall of the fault (Fig. 1a). Elastic dislocation modelling suggests over 80 cm of slip at depth on the fault (Fig. 1b–f). This area with high values of surface subsidence, and the implied area of high slip at depth, is located towards the southeastern end of the surface ruptures. Although some of this slip may be due to the 7th April Mw 5.6 aftershock (Papanikolaou et al., 2010), and we note that this event was not considered by the papers reviewed in Fig. 1, below we argue that non-planarity of the fault plane may have a role to play in producing these maxima skewed to the SE. Unfortunately, the surface ruptures occur in unconsolidated slope sediments in most places, so the orientation of the fault plane and the slip vectors of the earthquake are relatively poorly constrained, except in the central portion of the rupture within the town of Paganica where a study of offset tarmac and concrete surfaces along the rupture revealed that the slip vector plunges at 21° towards 218° (±5°), almost perpendicular to the strike of the fault (127°), at least at the surface (Roberts et al., 2010). The relatively poor exposure of the ruptures to the 2009 earthquake, especially in the region of the relay zone along the surface ruptures (R in Fig. 1a), led us to study the kinematics of neighbouring active normal faults. Below we report a study of the nearby Campo Felice fault (Figs. 2 and 3) accomplished using terrestrial laser scanning (TLS) and field structural mapping and analysis.

3. Methods

A TLS point cloud dataset of the Campo Felice fault was acquired using a Riegl LMS-z420i laser scanner. The dataset consisted of six scan positions and 11 million measurement points, covering the 5 km long southeastern segment of the Campo Felice fault (Fig. 4a). The point clouds from each scan position were co-registered using the RiSCAN Pro processing software. This process unites point clouds from each scan position within 3D space. Geo-referencing was carried out

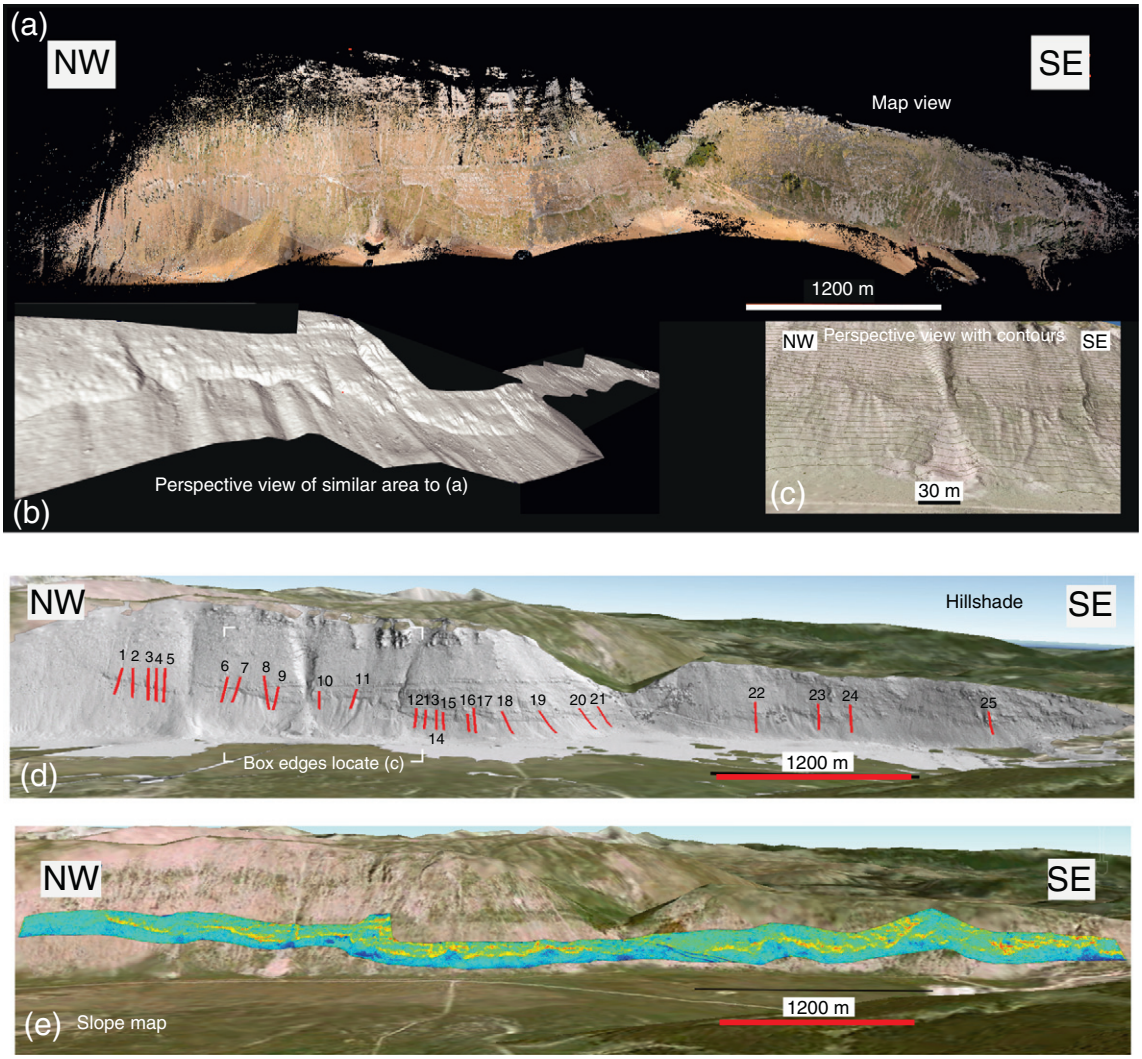

Fig. 4. LiDAR data, processing and analysis. (a) Point cloud data. (b) Manual removal of vegetation from point cloud. (c) Contour map located in (b). (d) TIN surface with the locations of 25 study sites where 10 scarp profiles were produced (250 scarp profiles in total). Each red line is actually 10 profile lines spaced 1 m apart along strike. A representative set of 25 scarp profiles from the 25 locations indicated are shown in Fig. 5. (e) A surface slope map using the slope calculation algorithm in goCAD and displayed in Google Earth. Blue colours correspond to low values of slope ~20 degrees. Yellow colours correspond to moderate values of slope ~40 degrees. Red colours correspond to high values of slope ~60 degrees.

by surveying a network of cylindrical reflectors present within each point cloud using real time kinematic (RTK) GPS. The vertical offsets that define the surface slip distribution can be recovered from these data following a number of data processing steps.

The point cloud dataset was filtered to remove vegetation using a combination of manual point removal and processing of the point cloud using the GEON *points2grid* pseudo-vegetation filter (Crosby et al., in review). A *points2grid* output point spacing of between 2–4 meters, with corresponding search radius R between 1.41–2.8 meters was found to be most suitable, as this preserves metre-scale changes in the ground surface whilst eradicating noise created by vegetation. Once the point cloud has been filtered to remove vegetation, a number of derivatives can be created from the dataset in order to identify geomorphic features.

Generation of a solid surface from a point cloud dataset facilitates study of the tectono-geomorphic features within the original point cloud dataset. A triangular irregular network (TIN) surface representation of the topography is created using Delaunay triangulation (Delaunay, 1934) with the vegetation-filtered pointset as input. Visualisation of the TIN surface in 3D, with lighting applied from a unidirectional source facilitates identification of geomorphic features of the faults scarps that are also studied in the field. These include the base of the fault scarp, the fault plane itself, colluvial wedges, the upper and lower geomorphic slopes, and footwall gullies and hanging wall erosional channels whose formation postdates formation of the upper and lower slopes (Fig. 4d and e).

A further enhancement to a TIN surface is to calculate the angle (slope) from horizontal of each triangle and to interpolate these data over the entire surface. These interpolated data can then be used to colour the surface according to the local slope creating a surface slope map (Fig. 4e), and to add topographic contours (Fig. 4c). Again, creation of a surface slope map with contours facilitates identification of the fault scarp and its constituent features. In particular, contours that are parallel, linear and equally spaced on the hanging wall and the footwall of the fault identify slopes from the last glacial maximum (LGM) that have been offset across the fault since 15 ± 3 ka (see Faure Walker et al., 2009 for an explanation). We used this to identify 25 sites where surface offsets have been produced solely by fault slip during earthquakes and not affected by geomorphic processes such as post 15 ka erosional gullying, colluvial and alluvial fan sedimentation or landslides. Topographic cross sections were generated at each of these 25 sites from the surface TIN. At each of the 25 sites ten topographic cross sections were created

Fig. 5. Scarp profiles derived from terrestrial laser scan data (TLS) from the 25 sites indicated in Fig. 4d, showing offsets of a 15 ± 3 ka periglacial slope. These 25 profiles are a sub-set of the 250 profiles generated to produce the values and error bars in Fig. 7. Offsets were interpreted using *Crossint*.

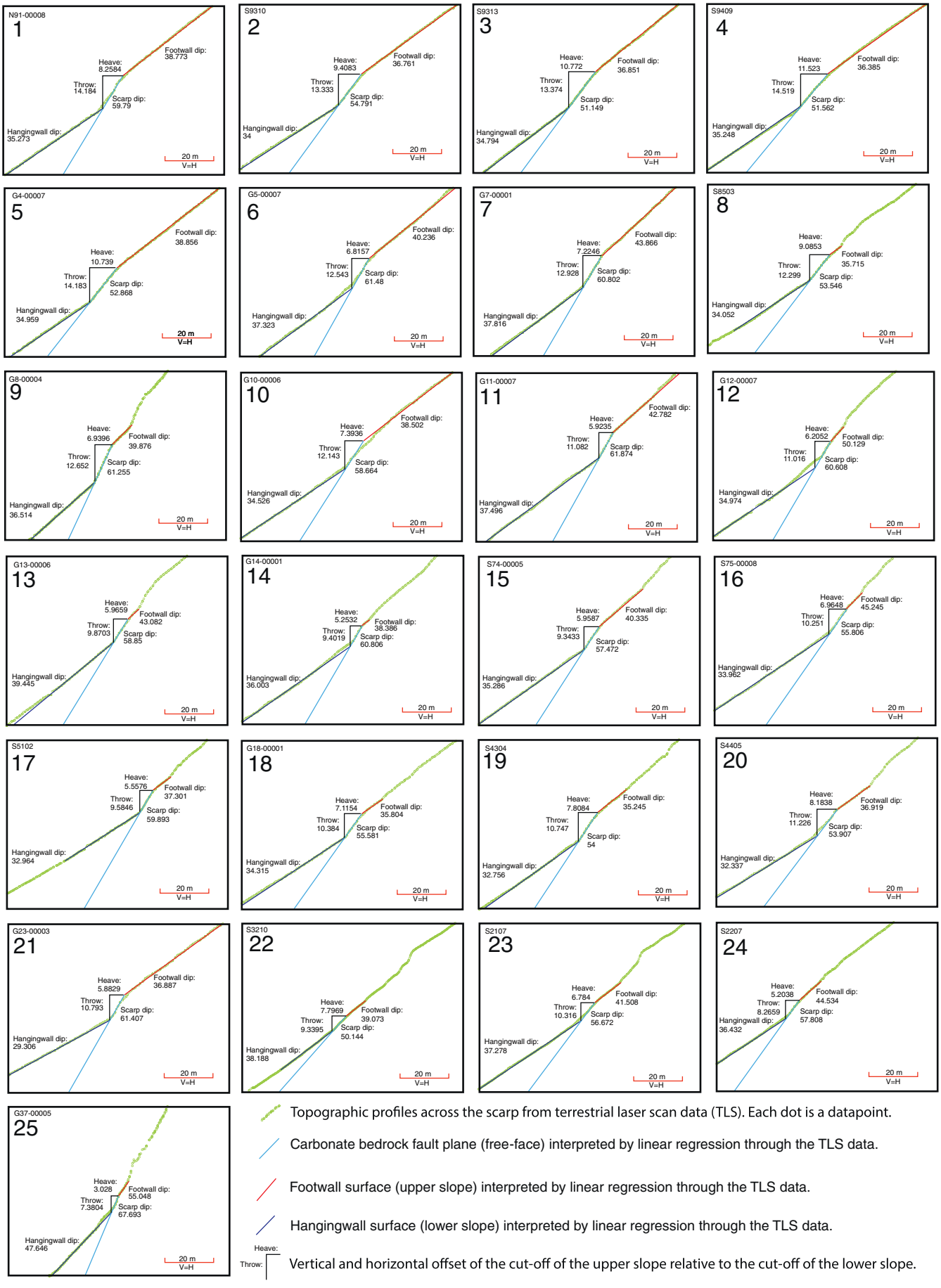
N91-00008
1
Heave: 8.2584
Throw: 14.184
Footwall dip: 38.773
Scarp dip: 59.79
Hangingwall dip: 35.273
S9310
2
Heave: 9.4083
Throw: 13.333
Footwall dip: 36.761
Scarp dip: 54.791
Hangingwall dip: 34
S9313
3
Heave: 10.772
Throw: 13.374
Footwall dip: 36.851
Scarp dip: 51.149
Hangingwall dip: 34.794
S9409
4
Heave: 11.523
Throw: 14.519
Footwall dip: 36.385
Scarp dip: 51.562
Hangingwall dip: 35.248
G4-00007
5
Heave: 10.739
Throw: 14.183
Footwall dip: 38.856
Scarp dip: 52.868
Hangingwall dip: 34.959
G5-00007
6
Heave: 6.8157
Throw: 12.543
Footwall dip: 40.236
Scarp dip: 61.48
Hangingwall dip: 37.323
G7-00001
7
Heave: 7.2246
Throw: 12.928
Footwall dip: 43.866
Scarp dip: 60.802
Hangingwall dip: 37.816
S8503
8
Heave: 9.0853
Throw: 12.299
Footwall dip: 35.715
Scarp dip: 53.546
Hangingwall dip: 34.052
G8-00004
9
Heave: 6.9396
Throw: 12.652
Footwall dip: 39.876
Scarp dip: 61.255
Hangingwall dip: 36.514
G10-00006
10
Heave: 7.3936
Throw: 12.143
Footwall dip: 38.502
Scarp dip: 58.664
Hangingwall dip: 34.526
G11-00007
11
Heave: 5.9235
Throw: 11.082
Footwall dip: 42.782
Scarp dip: 61.874
Hangingwall dip: 37.496
G12-00007
12
Heave: 6.2052
Throw: 11.016
Footwall dip: 50.129
Scarp dip: 60.608
Hangingwall dip: 34.974
G13-00006
13
Heave: 5.9659
Throw: 9.8703
Footwall dip: 43.082
Scarp dip: 58.85
Hangingwall dip: 39.445
G14-00001
14
Heave: 5.2532
Throw: 9.4019
Footwall dip: 38.386
Scarp dip: 60.806
Hangingwall dip: 36.003
S74-00005
15
Heave: 5.9587
Throw: 9.3433
Footwall dip: 40.335
Scarp dip: 57.472
Hangingwall dip: 35.286
S75-00008
16
Heave: 6.9648
Throw: 10.251
Footwall dip: 45.245
Scarp dip: 55.806
Hangingwall dip: 33.962
S5102
17
Heave: 5.5576
Throw: 9.5846
Footwall dip: 37.301
Scarp dip: 59.893
Hangingwall dip: 32.964
G18-00001
18
Heave: 7.1154
Throw: 10.384
Footwall dip: 35.804
Scarp dip: 55.581
Hangingwall dip: 34.315
S4304
19
Heave: 7.8084
Throw: 10.747
Footwall dip: 35.245
Scarp dip: 54
Hangingwall dip: 32.756
S4405
20
Heave: 8.1838
Throw: 11.226
Footwall dip: 36.919
Scarp dip: 53.907
Hangingwall dip: 32.337
G23-00003
21
Heave: 5.8829
Throw: 10.793
Footwall dip: 36.887
Scarp dip: 61.407
Hangingwall dip: 29.306
S3210
22
Heave: 7.7969
Throw: 9.3395
Footwall dip: 39.073
Scarp dip: 50.144
Hangingwall dip: 38.188
S2107
23
Heave: 6.784
Throw: 10.316
Footwall dip: 41.508
Scarp dip: 56.672
Hangingwall dip: 37.278
S2207
24
Heave: 5.2038
Throw: 8.2659
Footwall dip: 44.534
Scarp dip: 57.808
Hangingwall dip: 36.432
G37-00005
25
Heave: 3.028
Throw: 7.3804
Footwall dip: 55.048
Scarp dip: 67.693
Hangingwall dip: 47.646
20 m
V=H
Topographic profiles across the scarp from terrestrial laser scan data (TLS). Each dot is a datapoint.
Carbonate bedrock fault plane (free-face) interpreted by linear regression through the TLS data.
Footwall surface (upper slope) interpreted by linear regression through the TLS data.
Hangingwall surface (lower slope) interpreted by linear regression through the TLS data.
Heave:
Throw:
Vertical and horizontal offset of the cut-off of the upper slope relative to the cut-off of the lower slope.

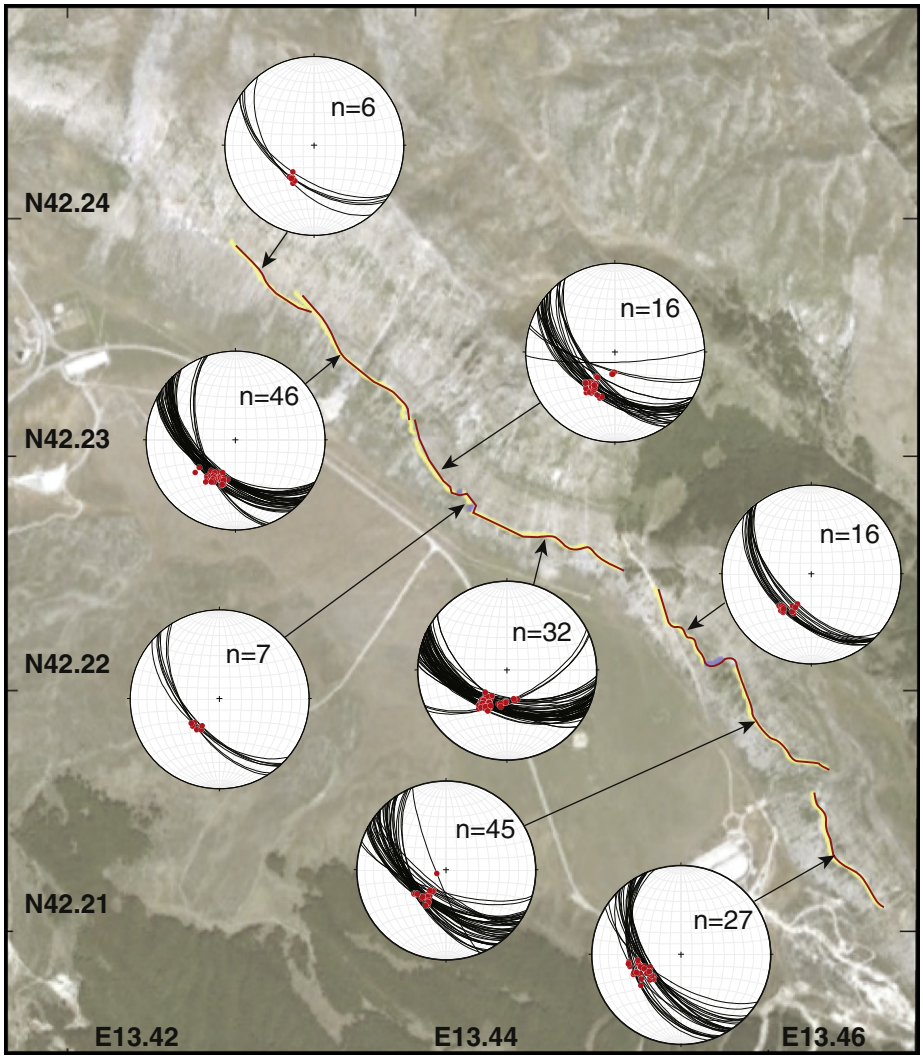

Fig. 6. Lower hemisphere stereographic projection of the orientation of fault planes and the slip-vector orientation defined by striated faults, showing how the kinematics of faulting vary along the Campo Felice fault. Data were collected from the 25 locations shown in Fig. 4.

in the direction of slip, spaced at 1 m intervals (Fig. 4d; 250 in total). Each of the topographic cross sections was interpreted for throw using the GNU/octave program *Crossint* (Fig. 5; see Electronic Supplement). A complete description of the functionality of *Crossint* can be found in Wilkinson (2012).

Throw was interpreted by manually picking representative portions of the hanging wall slope, fault plane and footwall slope from the topographic cross sections. *Crossint* performs linear regression of the data points between the picks to calculate the footwall-scarp and hanging wall-scarp intersections, from which the throw is calculated. This process was repeated for all 250 topographic cross sections.

Structural field measurements comprising strike, dip, slip-direction and plunge of the slip direction were collected along the entire length of the Campo Felice fault (Fig. 6). These field measurements were taken using a compass clinometer with locations provided by real time kinematic GPS with centimetre precision. In order to visualise the changing geometry and slip direction of the fault along its length, the GPS locations were converted to distance along the fault, from the northwestern end, to be plotted on the x-axis against the various measurements from the TLS analysis.

A strain-rate profile was calculated from data for throw, fault geometry and slip, using the method described by Faure Walker et al. (2009) (Fig. 7; Table 1). The advantage of converting to strain-rate compared to throw-rate is that the former takes into account variations in fault geometry and the direction of slip, as shown by Faure Walker et al. (2009). Strain-rate was calculated for boxed shaped areas using the equations below, as defined by Faure Walker et al. (2009). The components of strain e_{11}, e_{12} and e_{22} were calculated for each sample box of width L and area a. T represents the average throw measured on the fault within the sample box and t is the time period over which that throw has formed (for instance 15 ± 3 kyrs in the case of post glacial faulting in the central Apennines). The average values of plunge direction (*plunge*), slip direction (*slipdir*) and strike (*strike*) for field measurements within the sample box were also used. The direction of principal strain for each box is defined by θ. The principal strain-rate for each box (*strainrate*) was calculated in the direction of the regional principal strain direction (θ) for each sample box along the fault.

$$e_{11} = \frac{1}{at} LT \cot(plunge) \sin(slipdir) \cos(strike)$$

$$e_{22} = \frac{-1}{at} LT \cot(plunge) \cos(slipdir) \sin(strike)$$

$$e_{12} = \frac{1}{2at} LT \cot(plunge) \cos(slipdir + strike)$$

$$\theta = \frac{\arctan\left(2\frac{e_{12}}{e_{11}-e_{22}}\right)}{2}$$

$$strainrate = \frac{e_{11}+e_{22}}{2} - \frac{e_{11}+e_{22}}{2}\cos(2\theta_{ave}) - e_{12}\sin(2\theta_{ave})$$

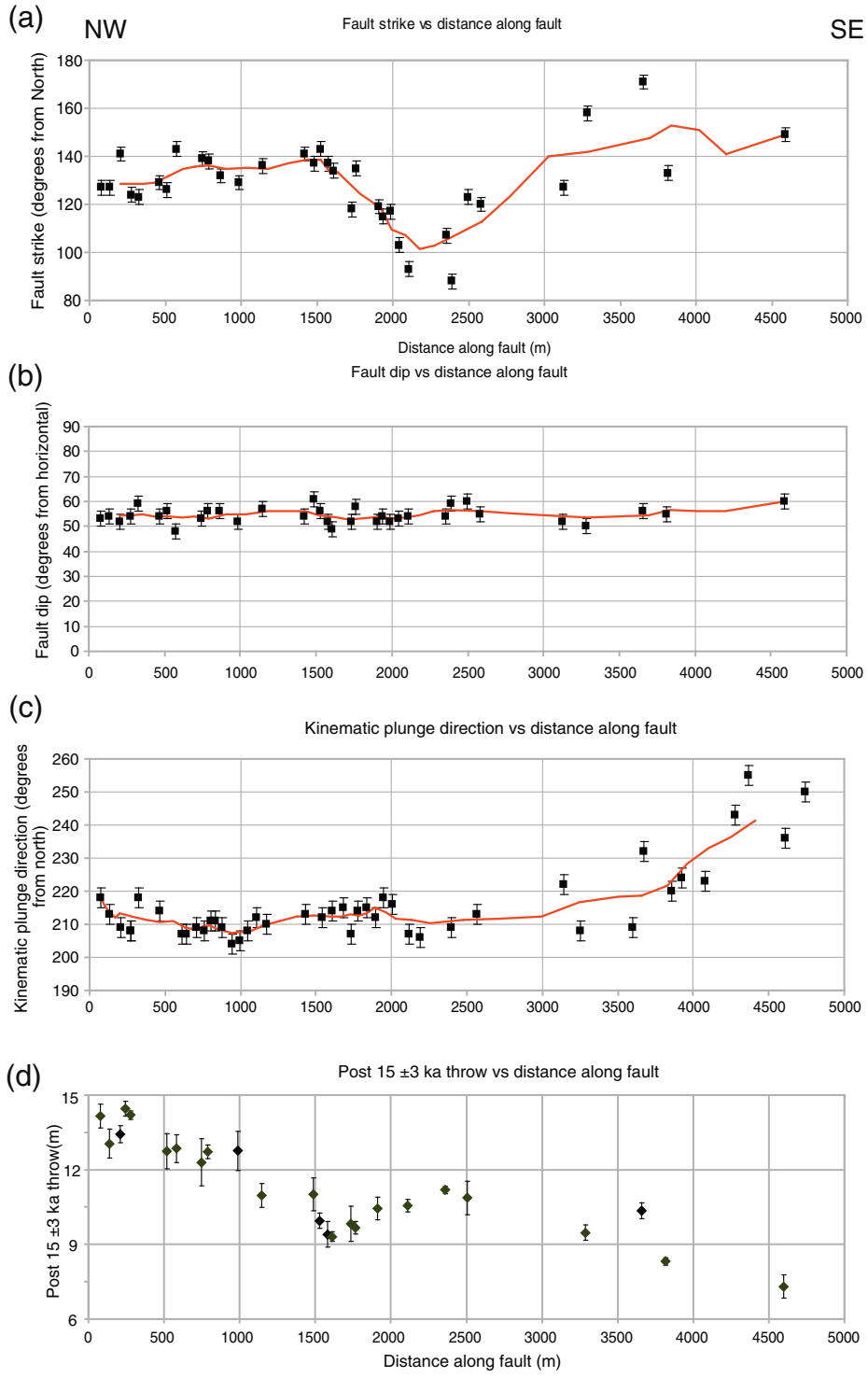

Fig. 7. Graphs showing the relationship between fault orientation and measures of the rate of faulting for the Campo Felice fault. (a) Fault strike. Error bars are ±3°. The red line is a moving point average of five measurements. The bend in the fault map trace occurs between 1500 and 2500 m along strike. (b) Fault dip. Error bars are ±3°. The red line is a moving point average of five measurements. (c) Slip direction. Error bars are ±3°. The red line is a moving point average of five measurements. (d) Post 15 ± 3 ka throw measured with TLS. (e) Throw and principal horizontal strain-rate (see Table 1). Strain-rate was calculated in 250 x 250 m boxes using the equations in the text. The error bars for throw are ±1σ for measurements of throw alone, not including those for uncertainty in age, whilst those for strain-rate are ±2σ. A throw-rate scale is also shown on the y axis for 3 scenarios for the age of the offset slope (12 ka, 15 ka and 18 ka) – our preferred estimate of the age is 15 ± 3 as it encompasses our assessment of the uncertainty (see Faure Walker et al., 2010 for discussion). (f) and (g) vertical offsets associated with two palaeo earthquakes recorded by stripes of freshly-exposed fault plane at the base of the exposed fault plane reported by Giaccio et al. (2002), but modified slightly during our own fieldwork. Errors on field estimates of the throw for these palaeo earthquakes are estimated to be ± 0.1 m. Overall, this figure shows that the throw-rate increases in the region of the change in fault strike to maintain the gradual decrease in strain-rate towards the fault tip.

4. Results

Fig. 7 shows how strike, dip, slip direction, throw-rate, strain-rate and coseismic slip vary along the studied segment of the Campo Felice fault. The measurements for fault strike (Fig. 7a) show a clear anomaly in fault strike between 1500 and 3000 m along the studied portion of the fault, consistent with the presence of a bend in the map trace of the fault. In contrast, field measurements of

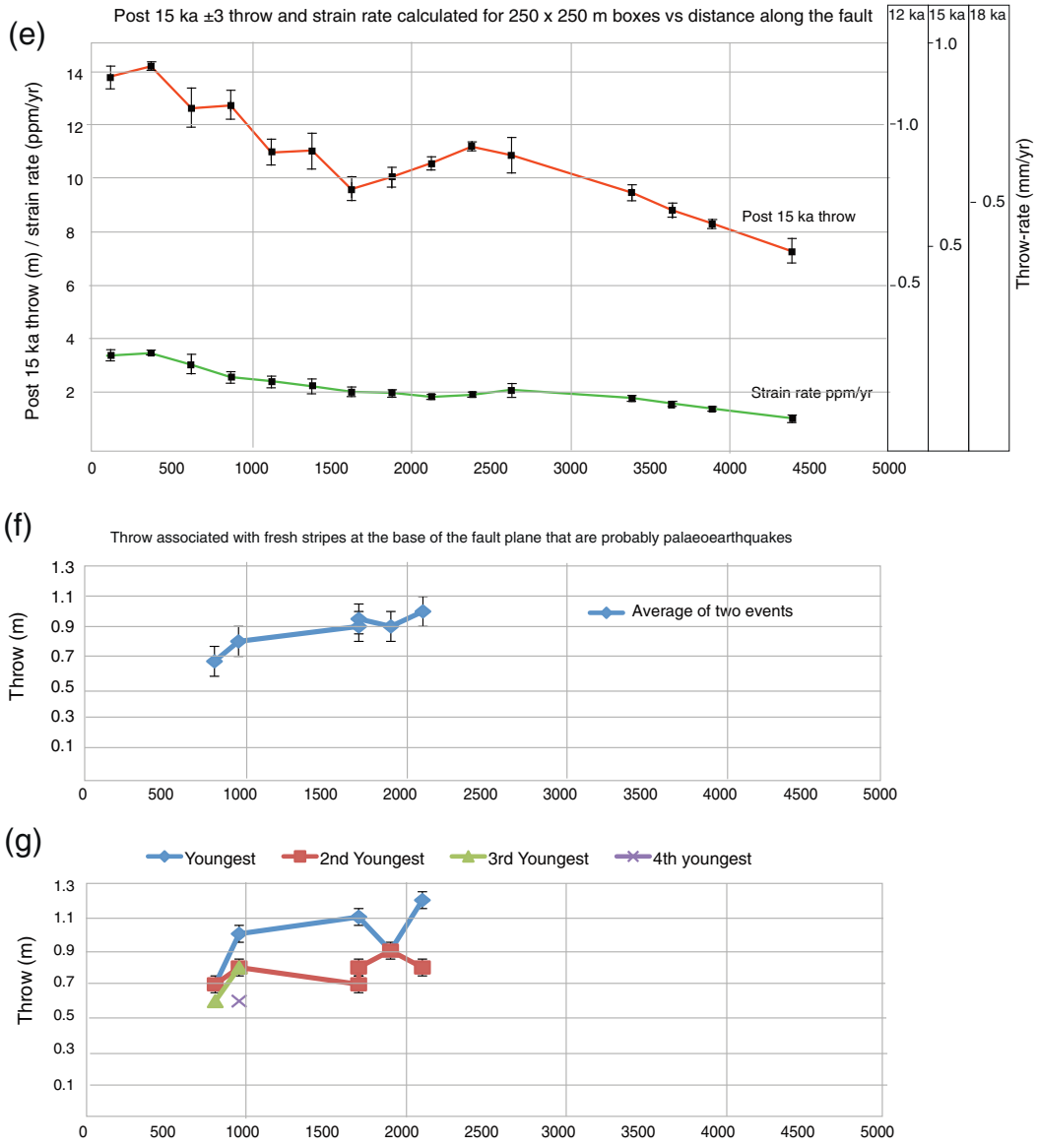

Fig. 7 (*continued*).

fault dip are consistent along the length of the fault (Fig. 7b). Field measurements for the direction of slip (Fig. 7c) are consistent between 0–3000 m distance along the fault, with a mean slip direction of 211° ($\pm 1\sigma = 3.9$). The slip direction becomes increasing oblique towards the southeastern tip, as is typical of normal faults (Roberts, 1996a, 1996b, 2007). The direction of slip increases from ~211° at

Table 1
Data used to calculate strain-rate in 250 m bins along strike.

Plunge of slip vector (degrees from horizontal)	Strike of fault (degrees from north)	Slip direction (degrees from north)	Throw (m)	Distance along strike (m)	Strain-rate (ppm/yr)
47	128	213	13.77	125	3.41
47	129	213	14.19	375	3.52
47	134	208	12.63	625	3.08
52	136	208	12.74	875	2.59
50	135	210	10.98	1125	2.42
52	138	213	11.02	1375	2.25
51	134	212	9.62	1625	2.05
53	118	215	10.05	1875	1.99
54	104	210	10.55	2125	1.86
55	105	209	11.19	2375	1.91
53	113	209	10.87	2625	2.09
53	142	208	9.47	3375	1.82
54	148	221	8.80	3625	1.60
55	153	222	8.31	3875	1.39
55	153	249	7.30	4375	1.04

3000 m distance along the fault to ~250° at the tip at 4750 m distance along the fault.

Interpretation of throw from 25 cross section locations (250 individual scarp profiles) using *Crossint* produced a post 15 ± 3 ka throw profile for the studied portion of the Campo Felice fault (Fig. 7d). The throw profile shows 1σ precisions for measurement of throw calculated from the mean and standard deviation of throw for the ten individual scarp profiles at each of the 25 locations. The throw profile describes a gradual increase in post 15 ± 3 ka throw along strike from close to zero at the fault tip (located at ~5000 m on Fig. 7d), through a value of ~7 m where the fault scarp begins to have a clear geomorphic expression to ~14 m at the northwestern end of the studied portion of the fault. We estimate that, given well-preserved morphology, it would be possible to identify scarps with throws as small as 1–2 metres. However, the exposure close to the southwestern fault tip has been degraded by mass-wasting and in this instance we have not been able to measure offsets right up to the fault tip. Superimposed on this general increase in post 15 ± 3 ka throw from southeast to northwest is a local increase between 1500–3500 m distance along the fault (Fig. 7d). The local increase reaches a maximum of ~11 m at ~2400 m distance along the fault, representing a 17% increase in relation to the value of ~9.5 m depicted at the local minimum at ~1600 m distance. This local increase in throw coincides geographically with the prominent bend in the trace of the fault (Fig. 7a).

In order to calculate strain-rates we have discretised the post 15 ± 3 ka throw data in Fig. 7d into 250 m sections of the faults (Fig. 7e). Strain rates decrease in an almost linear fashion from a maximum of ~3.51 ppm/yr at the northwestern exposed end of the Campo Felice fault to ~1.04 ppm/yr close to the tip at the southeastern end of the fault, in contrast to the strike and throw data which both show an anomaly between 1500-3000 m along strike.

We have also examined the vertical offsets produced by what appear to be at least two palaeo earthquakes along the portion of the fault we have studied (Fig. 7f and g). Giaccio et al. (2002) identified colour banding at the base of the exposed fault planes defined by variations in colour, erosion and moss/lichen density. Through analogy with other fault planes that display similar colour bands, which are known to have been produced by earthquake surface rupturing in historical earthquakes (e.g. Roberts, 1996b; Galli et al., 2008), they interpreted the presence of at least two palaeo earthquakes, defining vertical offsets as large as 1.2 m. Up to four stripes were noted by Giaccio et al. (2002), but only the two lowest can be correlated along strike for a significant distance. We have interpreted coseismic throws for these two palaeo earthquakes from examination of the data in Giaccio et al. (2002) and from our own field observations (Fig. 7f and g). Both the lowest (youngest) and penultimate event show increases in throw along strike, coincident with the position of the prominent bend in the fault trace. The average throw for both earthquakes increases from 0.66 ± 0.1 m to 1.0 ± 0.1 m along strike. Thus, in the vicinity of the prominent bend in the fault trace, both the cumulative throw that has accumulated since 15 ka, and the throw associated with two palaeo earthquakes over an unknown, but presumably shorter time period, depart from the pattern of gradual decrease towards the fault tip.

5. Discussion

Our main finding is that an anomaly in the orientation of the Campo Felice fault plane (a change in fault strike around a bend in the fault in this case) has produced a local maximum in fault throw since 15 ± 3 ka and hence throw rate over this time period, even though the strain-rate represented by the faulting shows a simple, almost linear decrease towards the fault tip. This pattern can be recognised over the timescale of faulting since the last glacial maximum (15 ± 3 ka) and over the timescale of two palaeo earthquakes (much less than 15,000 years). The local anomaly in throw-rate on the Campo Felice fault is elevated by ~0.2 mm/yr (~33%) relative to the value expected (assuming slip since 15 ka), given a linear extrapolation of the value towards the fault tip. This is ~40% of the total variation in recorded throw-rate on the studied portion of the fault (range is 0.95-0.45 mm/yr; that is, 0.5 mm/yr).

A similar pattern of increased throw-rate on a fault bend was recorded by Faure Walker et al. (2009), but in much less detail. The throw-rate doubled along part of the Parasano fault where the obliquity of the fault strike relative to the slip-vector increased by ~30° and the fault dip increased by ~6°. However, in the example described here from the Campo Felice Fault, the fault dip remains relatively constant across the bend. Taking the Parasano and Campo Felice examples together, we conclude that relatively small variations in fault orientation have significant effects on the vertical motions associated with the surface slip distribution. Some evidence exists that this is a common feature of active faulting. For example, Taylor et al. (2004) recorded a significant increase in fault throw in the location of a fault bend on the Rangitaiki fault (offshore, Bay of Plenty, New Zealand) from seismic reflection data. However, the lack of slip-direction data in that study does not allow the increase in throw to be quantitatively attributed to changes in fault geometry as we have achieved in this paper.

This leads to the question of what effect variations in fault orientation have on slip at depth. A prominent feature of the deformation associated with the 2009 Mw 6.3 L'Aquila earthquake (Fig. 1), are that the maximum surface subsidence and modelled subsurface slip is skewed in location towards the south east relative to the overall rupture location, where a 1–2 km-wide relay zone exists between two portions of the surface rupture. We note that all five studies of subsurface slip distribution illustrated in Fig. 1 have chosen to model the deformation with a single fault at depth despite observations of the relay zone. If a single fault at depth is to link to segmented faults at the surface, as suggested by Calderoni et al. (2012), a significant bend of the fault surface must exist in the subsurface with an along strike extent of ~4 km and an across strike amplitude of ~2 km (Fig. 8). This bend is significantly larger than the example we have measured on the Campo Felice Fault (~0.6 km by ~0.4 km) and also larger than the example on the Parasano Fault described by Faure Walker et al. (2009) (~1 km by ~0.8 km). We suggest that it is likely that this 4 × 2 km bend in the subsurface fault trace will have affected the magnitude of slip on the fault plane in the 2009 earthquake to produce an anomalous patch of relatively-high vertical motion (subsidence). Through analogy with the Campo Felice fault, the vertical motion could have been tens of percent more than what would have been produced if the fault plane had been planar. The implications of this are as follows:

1) The modelled slip distributions shown in Fig. 1 are useful in that they allow visualisation of the relationship between surface deformation and slip at depth. However, in detail it is clear that if deviations from planarity of a ruptured fault are not considered the modelled slip distribution is a simplification of the actual slip on the fault.
2) The relationship between vertical motions at the surface, slip at depth and the derived earthquake moment magnitude will be affected by non-planarity of the fault and the resultant simplification of the modelled slip. The seismic moment of an earthquake is calculated by combining values for the dimensions of the rupture, the stiffness of the ruptured material and the amount of slip (Kostrov, 1974). If the slip at depth is simplified due to non-planarity of the fault plane that is omitted from the modelling, and that value for slip at depth is used in calculations of seismic moment, the derived value for seismic moment will be affected. This also applies to attempts to relate slip at the surface in historical earthquake ruptures to moment magnitude. The extremely useful and widely-used database presented by Wells and Coppersmith (1994) does not include data on whether surface slip was taken from parts of the fault with orientations that typify the overall rupture or from local anomalies with atypical fault orientations in local bends or relay zones. We

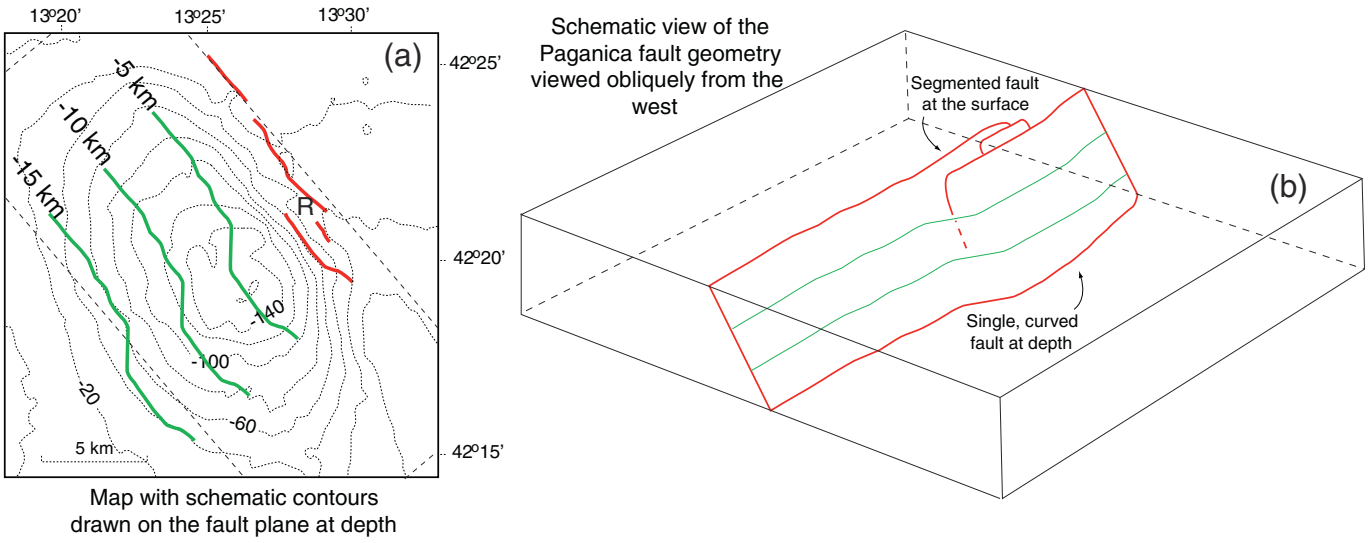

Fig. 8. Summary cartoon showing how the location of maximum coseismic subsidence associated with the 2009 L'Aquila Earthquake (Ms 6.3) may relate to the subsurface geometry of the fault. We speculate that the segmented fault at surface coalesces into a single curved fault at depth, and the along-strike bend in the fault requires high values for vertical motion following the relationships quantified by Faure Walker et al. (2009).

suggest this may be one of the reasons for scatter in the relationships between rupture length, slip and moment magnitudes in the database of Wells and Coppersmith (1994). Thus, the role of geometrical complexity is important and will influence the slip distribution (see Wesnousky, 2008).

3) Stress transfer modelling depends on using the slip distribution at depth from an earthquake to model the stress transfer to so-called "receiver faults" (e.g. Walters et al., 2009). If the modelled slip distribution is a simplification, the stress transfer will also be a simplification. If the modelled slip distribution on a planar fault has concentrations of high slip, that are an artefact of inverting measured anomalies in ground deformation at the surface with a simple planar fault, when in fact the fault is not a single plane, then the modelled concentrations of high stress will in turn be artefacts – yet it is these modelled concentrations of high stress on receiver faults that may cause concern in terms of the possibility of imminent slip in a triggered earthquake.
4) Palaeo seismological studies of past earthquakes commonly measure the throw per event and throw-rate associated with past events (Galli et al., 2008). However, it is rare for such studies to record the spatial variation in fault orientation around the palaeo seismic site, usually because the fault plane is poorly-exposed in the unconsolidated material associated with sites suitable for trenching. Importantly, we have shown that defining fault orientations is essential if the significance of the throw per event and throw-rate values are to be fully understood. For example, the coseismic throw implied by colour stripes on the Campo Felice Fault may be overestimated by ~30% compared to values outside the local fault bend (Fig. 7); using the maximum value without understanding that it is generated by a local anomaly in fault orientation leads to overestimation of the moment magnitude and hence the rupture length. As rupture dimensions and maximum earthquake magnitudes are used for seismic hazard and engineering design purposes, local changes in fault orientation should be taken into account.

The implications listed above are profound for our understanding of the earthquake process, yet to date we only have two examples where the anomalous slip produced by bends in a fault plane have been quantified (this study and Faure Walker et al., 2009). We suggest that more studies of the geomorphology and structural geology of active faults are needed to produce an empirical relationship between the dimensions of bends in fault planes and the amplitude of vertical deformation.

6. Conclusions

A study of the structural geology and geomorphology of the well-exposed Campo Felice active normal fault shows that despite a simple linear decrease in strain-rate along strike from the fault centre to tip, a change in fault strike has produced a localised anomaly in vertical motion, with the throw-rate increasing by ~30-40% close to the fault bend. The throw anomaly can be resolved both over a timescale of multiple seismic cycles (15 ± 3 ka in this case) or over the timescale of two individual palaeo earthquakes (<15 kyrs). This example is well explained by theoretical considerations advanced by Faure Walker et al. (2009), who show that horizontal strain-rates and rates of vertical and horizontal deformation are linked by variables that include fault slip vectors and fault orientations. A 4 × 2 km relay zone in the surface ruptures to the 2009 L'Aquila earthquake (Mw 6.3) on the neighbouring Paganica fault is likely to be underlain by a bend in the fault trace at depth of similar dimensions. The theory of Faure Walker et al. (2009) suggests that a bend of this size will produce a significant local anomaly in throw per event and throw-rate on the fault. Surface deformation for this earthquake is skewed towards the southeastern end of the rupture trace, with a maximum in the vicinity of the aforementioned relay zone. Existing attempts to model this deformation have used a planar fault, but we suggest that improved models of the subsurface slip distributions will be achieved if a non-planar fault with a change in strike is utilised. Surface and subsurface slip distributions are used to model stress transfer and calculate maximum magnitudes for palaeo earthquakes. We suggest the orientation of the fault plane in question should be considered with care as uncertainty in fault plane orientation relative to the slip-vector will produce uncertainty in derived stress transfer and maximum magnitude estimates. Study of the geomorphology and structural geology of faults at surface is therefore a key input in order to properly define fault activity for the purpose of accurate seismic hazard assessment.

Acknowledgements

This work was funded by NERC Grants NE/H003266/1, NE/E01545X/1, NE/B504165/1, GR9/02995 and NE/I024127/1, a studentship to J.P. Faure Walker (NER/S/A/2006/14042). Maxwell Wilkinson was supported by a Durham Doctoral Scholarship.

Appendix A. Supplementary data

Supplementary data to this article can be found online at http://dx.doi.org/10.1016/j.geomorph.2014.04.026.

References

Atzori, S., Hunstad, I., Chini, M., Salvi, S., Tolomei, C., Bignami, C., Stramondo, S., Trasatti, E., Antonioli, A., Boschi, E., 2009. Finite fault inversion of DInSAR coseismic displacement of the 2009 L'Aquila earthquake (central Italy). Geophys. Res. Lett. 36. http://dx.doi.org/10.1029/2009GL039293 (L15305).

Boncio, P., Pizzi, A., Brozzetti, G., Pomposo, G., Lavecchia, G., Di Naccio, D., Ferrarini, F., 2010. Coseismic ground deformation of the 6 April 2009 L'Aquila earthquake (central Italy, Mw6.3). Geophys. Res. Lett. 37, L06308. http://dx.doi.org/10.1029/2010GL042807.

Calderoni, G., Di Giovambattista, R., Vannoli, P., Pucillo, S., Rovelli, A., 2012. Fault-trapped waves depict continuity of the fault system responsible for the 6 April 2009 Mw 6.3 L'Aquila earthquake, central Italy. Earth Planet. Sci. Lett. 323–324, 1–8.

Chan, Y.-C., Chen, Y.-G., Shih, T.-Y., Huang, C., 2007. Characterizing the Hsincheng active fault in northern Taiwan using airborne LiDAR data: Detailed geomorphic features and their structural implications. J. Asian Earth Sci. 31, 303–316. http://dx.doi.org/10.1016/j.jseaes.2006.07.029.

Cheloni, D., D'Agostino, N., D'Anastasio, E., Avallone, A., Mantenuto, S., Giuliani, R., Mattone, M., Calcaterra, S., Gambino, P., Dominici, D., Radicioni, F., Fastellini, G., 2010. Coseismic and initial post-seismic slip of the 2009 Mw6.3 L'Aquila earthquake, Italy, from GPS measurements. Geophys. J. Int. 181, 1539–1546. http://dx.doi.org/10.1111/j.1365-246X.2010.04584.x.

Cirella, A., Piatanesi, A., Cocco, M., Tinti, E., Scognamiglio, L., Michelini, A., Lomax, A., Boschi, E., 2009. Rupture history of the 2009 L'Aquila (Italy) earthquake from non-linear joint inversion of strong motion and GPS data. Geophys. Res. Lett. 36. http://dx.doi.org/10.1029/2009GL039795 (L19304).

Cowie, P.A., Scholz, C.H., Roberts, G.P., Faure Walker, J.P., Steer, P., 2013. Viscous roots of active seismogenic faults revealed by geologic slip rate variations. Nat. Geosci. 6, 1036–1040. http://dx.doi.org/10.1038/NGEO1991 (3rd November 2013).

Crosby, C.J., Krishnan, S., Arrowsmith, J.R., Kim, H.S., Colunga, J., Alex, N., Baru, B., 2014. Points2Grid: An Efficient Local Gridding Method for DEM Generation from Lidar Point Cloud Data. Geosphere special issue on Applications of Lidar in the Earth Sciences (in review).

D'Agostino, N., Jackson, J., Dramis, F., Funiciello, R., 2001. Interactions between mantle upwelling, drainage evolution and active normal faulting: an example from the central Apennines (Italy). Geophys. J. Int. 147, 475–497.

D'Agostino, N., Cheloni, D., Fornaro, G., Giuliani, R., Reale, D., 2012. Space-time distribution of afterslip following the 2009 L'Aquila earthquake. J. Geophys. Res. 117. http://dx.doi.org/10.1029/2011JB008523 (B02402).

Delaunay, B., 1934. Sur la sphère vide. Izvestia Akademii Nauk SSSR, 7. Otdelenie Matematicheskikh i Estestvennykh Nauk pp. 793–800.

Faure Walker, J.P., Roberts, G.P., Cowie, P.A., Papanikolaou, I., Sammonds, P.R., Michetti, A.M., Phillips, R.J., 2009. Horizontal strain-rates and throw-rates across breached relay zones, central Italy: Implications for the preservations of throw deficits at points of normal fault linkage. J. Struct. Geol. 31, 1145–1160.

Faure Walker, J.P., Roberts, G.P., Sammonds, P., Cowie, P.A., 2010. Comparison of earthquakes strains over 10^2 and 10^4 year timescales: insights into variability in the seismic cycle in the central Apennines, Italy. J. Geophys. Res. 115. http://dx.doi.org/10.1029/2009JB006462 (B10418).

Faure Walker, J.P., Roberts, G.P., Cowie, P.A., Papanikolaou, I., Michetti, A.M., Sammonds, P., Wilkinson, M., McCaffrey, K.J.W., Phillips, R., 2012. Relationship between topography and strain-rate in the actively-extending Italian Apennines. Earth Planet. Sci. Lett. 325–326, 76–84. http://dx.doi.org/10.1016/j.epsl.2012.01.028.

Galadini, F., Galli, P., 2000. Active Tectonics in the Central Apennines (Italy) - Input Data for Seismic Hazard Assessment. Nat. Hazards 22, 225–270.

Galli, P., Galadini, F., Pantosti, D., 2008. Twenty years of paleoseismology in Italy. Earth-Sci. Rev. 88, 89–117.

Giaccio, B., Galadini, F., Sposato, A., Messina, P., Moro, M., Zreda, M., Cittadini, A., Salvi, S., Todero, A., 2002. Image processing and roughness analysis of exposed bedrock fault planes as a tool for paleoseismological analysis: results from the Campo Felice fault (central Apennines, Italy). Geomorphology 49, 281–301.

Giraudi, C., Bodrato, G., Lucchi, M.R., Cipriani, N., Villa, I.M., Giaccio, B., Zuppi, G.M., 2011. Middle and late Pleistocene glaciations in the Campo Felice Basin (central Apennines, Italy). Quaternary Res. 75, 219–230.

Giraudi, C., 2012. The Campo Felice Late Pleistocene Glaciation (Apennines, Central Italy). J Quaternary Sci 27, 432–440.

Gold, R., Cowgill, E., Arrowsmith, J.R., Chen, X., Sharp, W.D., Cooper, K.M., Wang, X.F., 2011. Faulted terrace risers place new constraints on the late Quaternary slip rate for the central Altyn Tagh Fault, northwest Tibet. Geol. Soc. Am. Bull. 123, 958–978. http://dx.doi.org/10.1130/B30207.1.

Gold, P.O., Cowgill, E., Kreylos, O., Gold, R.D., 2012. A terrestrial lidar-based workflow for determining three-dimensional slip vectors and associated uncertainties. Geosphere 8, 431–442.

Kostrov, V.V., 1974. Seismic Moment and Energy of Earthquakes, and Seismic Flow of Rock, Izv. Earth Phys. 1, 23–40 (translation UDC 550.341, 13-21).

Michetti, A.M., Brunamonte, F., Serva, L., Vittori, E., 1996. Trench investigations of the 1915 Fucino earthquake fault scarps (Abruzzo, Central Italy): geological evidence of large historical events. J. Geophys. Res. 101 (B3), 5921–5936.

Oldow, J.S., Singleton, E.S., 2008. Application of Terrestrial Laser Scanning in determining the pattern of late Pleistocene and Holocene fault displacement from the offset of pluvial lake shorelines in the Alvord extensional basin, northern Great Basin, USA. Geosphere 4, 536–563.

Pace, B., Peruzza, L., Lavecchia, G., Boncio, P., 2006. Global seismogenic source modelling and probabilistic seismic hazard analysis in Central Italy. Bull. Seismol. Soc. Am. 96, 107–132.

Papanikolaou, I.D., Foumelis, M., Paracharidis, E.L., Lekkas, J., Fountoulis, G., 2010. Deformation pattern of the 6 and 7 April 2009, M = 6.3 and Mw 5.6 earthquakes in L'Aquila (central Italy) revealed by ground and space observations. Nat. Hazards Earth Syst. 10, 73–87.

Roberts, G.P., 1996a. Variation in fault-slip directions along active normal faults. J. Struct. Geol. 18, 835–845.

Roberts, G.P., 1996b. Noncharacteristic earthquake ruptures from the Gulf of Corinth, Greece. J. Geophys. Res. 101, 25255–25267.

Roberts, G.P., 2007. Fault orientation variations along the strike of active normal fault systems in Italy and Greece: Implications for predicting the orientations of subseismic-resolution faults in hydrocarbon reservoirs. Am. Assoc. Pet. Geol. Bull. 91 (1), 1–20.

Roberts, G.P., Michetti, A.M., 2004. Spatial and temporal variations in growth rates along active normal fault systems: an example from the Lazio-Abruzzo Apennines, central Italy. J. Struct. Geol. 26, 339–376.

Roberts, G.P., Raithatha, B., Sileo, G., Pizzi, A., Pucci, S., Faure Walker, J., Wilkinson, M., McCaffrey, K., Phillips, R.J., Michetti, A.M., Guerrieri, L., Blumetti, A.M., Vittori, E., Cowie, P.A., Sammonds, P., Galli, P., Boncio, P., Bristow, C., Walters, R., 2010. Shallow sub-surface structure of the 6th April 2009 Mw 6.3 L'Aquila earthquake surface rupture at Paganica, investigated with Ground Penetrating Radar. Geophys. J. Int. 183, 774–790. http://dx.doi.org/10.1111/j.1365-246X.2010.04713.x.

Taylor, S., Bull, B., Lamarche, G., Barnes, P., 2004. Normal fault growth and linkage in the Whakatane Graben, New Zealand, during the last 1.3 Myr. J. Geophys. Res. 109, B02408. http://dx.doi.org/10.1029/2003JB002412.

Vezzani, L., Ghisetti, F., 1998. Carta Geologica Dell'Abruzzo, 1:100000, SELCA, Firenze.

Vittori, E., Di Manna, P., Blumetti, A.M., Comerci, V., Guerrieri, L., Esposito, E., Michetti, A.M., Porfido, S., Piccardi, L., Roberts, G., Berlusconi, A., Livio, F., Sileo, G., Wilkinson, M., McCaffrey, K., Phillips, R., Cowie, P.A., 2011. Surface faulting of the April 6, 2009, Mw 6.3 L'Aquila earthquake in Central Italy. Bull. Seismol. Soc. Am. 101, 1507–1530. http://dx.doi.org/10.1785/0120100140.

Walters, R.J., Elliott, J.R., D'Agostino, N., England, P.C., Hunstad, I., Jackson, J.A., Parsons, B., Phillips, R.J., Roberts, G.P., 2009. The 2009 L'Aquila earthquake (central Italy): A source mechanism and implications for seismic hazard. Geophys. Res. Lett. 36. http://dx.doi.org/10.1029/2009GL039337 (L17312).

Wells, D.L., Coppersmith, K.J., 1994. New empirical relationships among magnitude, rupture length, rupture width, rupture area and surface displacement. Bull. Seismol. Soc. Am. 84, 974–1002.

Wesnousky, S.G., 2006. Predicting the endpoints of earthquake ruptures. Nature 444, 358–360. http://dx.doi.org/10.1038/nature05275.

Wesnousky, S.G., 2008. Displacement and geometrical characteristics of earthquake surface ruptures: issues and implications for seismic-hazard analysis and the process of earthquake rupture. Bull. Seismol. Soc. Am. 98 (4), 1609–1632. http://dx.doi.org/10.1785/0120070111.

Wiatr, T., Reicherter, K., Papanikolaou, I., Fernández-Steeger, T., Mason, J., 2013. Slip vector analysis with high resolution t-LiDAR scanning. Tectonophysics 608, 947–957.

Wilkinson, M.W., 2012. The use of Terrestrial Laser Scanning in characterizing active tectonic processes from postseismic slip to the long term growth of normal faults. (Doctoral thesis) Durham University (http://etheses.dur.ac.uk/5573/).

Zielke, O., Arrowsmith, J.R., 2012. LaDiCaoz and LiDARimager -MATLAB GUIs for LiDAR data handling and lateral displacement measurement. Geosphere 8 (1), 206–221. http://dx.doi.org/10.1130/GES00686.1.

Zielke, O., Arrowsmith, J.R., Grant-Ludwig, L.B., Akciz, O.S., 2010. Slip in the 1857 and earlier large earthquakes along the Carrizo segment, San Andreas Fault. Science 327, 1119–1122. http://dx.doi.org/10.1126/science.1182781.